Electronic and mechanical properties of Sc*X*I (*X* = S, Se) monolayers and their heterostructures

Lixiang Rao,[1] Gang Tang ☉,[2,*] and Jiawang Hong[1,†]

[1]*School of Aerospace Engineering, Beijing Institute of Technology, Beijing 100081, China*
[2]*Advanced Research Institute of Multidisciplinary Science, Beijing Institute of Technology, Beijing 100081, China*

Inspired by the successful synthesis of bulk ScSI in a recent work [Ferrenti *et al.*, Chem. Mater. **34**, 5443 (2022)], we have systematically investigated the mechanical and electronic properties of Sc*X*I (*X* = S, Se) monolayers and their heterostructures by using first-principles calculations. Our calculations verify the experimental speculation that the bulk ScSI is readily exfoliatable and the monolayers of Sc*X*I (*X* = S, Se) are stable. The Young's moduli with strong anisotropy (50.2–91.5 N m^{-1}) of Sc*X*I monolayers are comparable to those of phosphorene (26–105 N m^{-1}), but smaller than those of isotropic graphene (349 N m^{-1}), MoS$_2$ (122.3 N m^{-1}), and *h*-BN (276 N m^{-1}), indicating their lower stiffness. In addition, ScSI/ScSeI monolayers show good flexibility with critical strain of 29%/33%. Application of strain can effectively regulate the band gap (E_g) and band edge of Sc*X*I (*X* = S, Se) monolayers. For instance, the E_g of the ScSeI monolayer is reduced from 1.83 to 1.59 eV and the band gap type is changed from indirect to direct band gap when a compressive strain of 6% is applied along the *x* direction, which is attributed to the orbital hybridization between the *d* orbital of Sc and *p* orbital of the elements at the *X* and I sites. More importantly, Sc*X*I (*X* = S, Se) monolayers can form type II vertical heterostructure with typical two-dimensional semiconductors due to the deeper energy levels of their valence band maximum and conduction band minimum. In addition, Sc*X*I (*X* = S, Se) monolayers can also be used to form type I lateral heterostructure with the ScSeBr monolayer. The excellent ductility, strain-tuned electronic properties, and heterostructure design make Sc*X*I (*X* = S, Se) monolayers promising candidates for the application of flexible electronic devices.

I. INTRODUCTION

Since the successful preparation of graphene in 2004 [1], more and more families of two-dimensional (2D) material, such as mono-elemental crystals (Xenes, e.g., phosphorene, borophenes), transition metal dichalcogenides [(TMDCs), e.g., MoS$_2$, TaSe$_2$], and group III-V semiconductors (e.g., GaN, BN), have been successfully discovered [2–7]. Two-dimensional materials with the FeOCl-type structure, as one of the most common 2D structural prototypes, have also attracted wide attention because of their wonderful opto-electronics, photovoltaics, and topological properties [8–10]. Compared with monoelemental and binary 2D materials, ternary 2D materials with FeOCl-type structure hold more element combinations to produce diverse properties. For instance, the 2D *MOX* (*M* = Sc, Ti, V, Cr, Fe; *X* = Cl, Br) materials exhibit different magnetic behaviors by regulating and controlling different numbers of 3*d* electrons in the M^{3+} ions with change in composition of the *M* site [8], which are potential candidates for spin-dependent electronic and opto-electronic devices. Single-layer *M*N*X*s (*M* = Ti, Zr, Hf; *X* = Cl, Br, I) with FeOCl structure are a series of semiconductor materials with desirable band gaps (1.55–2.69 eV) [11], hold-

ing promise as candidates for applications in photocatalytic water splitting.

In addition to the several types of FeOCl structures mentioned earlier, there is another class of FeOCl structures, RESI (RE = rare earth), that has attracted a lot of attention because they exhibit excellent semimetallic, topological, and magnetic properties [12–15]. In the RESI family of materials, they show a diverse range of structural phases from *Pcab* to *R*-3*m* to *Pmmn* with the decrease of the size of the metal cation from 1.032 (La) to 0.861 (Lu) Å. When RE = Y, Gd-Lu with ionic radius below 0.94 Å, RESI structures hold the FeOCl structure type under standard pressure conditions [12]. Among rare-earth atoms, the Sc atom has the smallest ionic radius (0.745 Å) and it can be speculated that ScSI structure is most likely to have the FeOCl structure type, but its synthesis has been delayed so that its structure type also remains uncertain. Very recently, Ferrenti *et al.* [12] successfully synthesized a new semiconductor, ScSI (space group *Pmmn*, No. 59), with a large indirect band gap of 2.0 eV. It is speculated that this material is very easy to exfoliate and has the potential to be applied in the field of heterojunctions. However, there is a lack of theoretical studies to verify that ScSI monolayers are stable and can be applied in the field of heterojunctions.

In this work, we present a comprehensive theoretical study of the structural, mechanical, and electronic properties of Sc*X*I (*X* = S, Se) monolayers and their heterostructures using first-principles calculations. The paper is organized as

*gtang@bit.edu.cn
†hongjw@bit.edu.cn

TABLE I. The structural parameters (lattice constants a and b; bond lengths d_1, d_2, and d_3; buckling height h) and cohesive energy E_c of ScXI (X = S, Se) monolayers.

Structure	a (Å)	b (Å)	d_1 (Å)	d_2 (Å)	d_3 (Å)	h (Å)	E_c (eV/atom)
ScSI	3.886	5.045	2.574	2.542	2.875	6.24	−4.710
ScSeI	3.948	5.320	2.701	2.670	2.882	6.27	−3.499

follows. Firstly, the structure stability and chemical bond nature of ScXI (X = S, Se) monolayers are demonstrated. Secondly, the mechanical properties and tensile strength of ScXI (X = S, Se) monolayers are studied. Thirdly, the effect of the compressive strain on the band edges and band gap of ScXI (X = S, Se) monolayers is analyzed in detail. Finally, the electronic properties of ScSeI/GeS vertical and (ScSeI)$_3$/(ScSeBr)$_3$ lateral heterostructures are investigated.

II. COMPUTATIONAL METHOD

Density functional theory (DFT) calculations were performed using the Vienna *ab initio* Simulation Package (VASP) [16,17]. The projector-augmented wave (PAW) method and generalized gradient approximation (GGA) with the Perdew-Burke-Ernzerhof (PBE) functional [18] were adopted to describe the ion-electron interaction and the exchange-correlation part of the electron-electron interaction, respectively. A kinetic-energy cutoff of 400 eV was used for the plane-wave basis set to ensure convergence [19]. The crystal structures used in our calculations were optimized until the energy and force convergence were $\leqslant 10^{-6}$ eV and 0.01 eV/Å, respectively. The Brillouin zone was sampled with Monkhorst-Pack k-point meshes [20,21] with a reciprocal space resolution of $2\pi \times 0.045\,\text{Å}^{-1}$ for structural optimization. A vacuum layer of at least 18 Å was introduced along the z axis to avoid spurious interactions between periodic images. The van der Waals (vdW) correction proposed by the DFT-D3 approach in Grimme's scheme was chosen to describe the intralayer long-range interaction [22,23], which is in good agreement with the experimental lattice parameters of bulk ScSI (see Table I in the Supplemental Material [24]). The Heyd-Scuseria-Ernzerhof (HSE06) screened hybrid functional [25,26] was employed to obtain more accurate electronic properties. Here, the optimal HSE exact-exchange mixing ratio was determined based on the deviation between the experimental band gap and the HSE06-calculated band gap of bulk ScSI (see Fig. 1(a) in the Supplemental Material [24]). The effect of spin-orbit coupling (SOC) on the electronic band structure of the bulk ScSI is negligible, and is not included in our calculations (see Fig. 1(b) in the Supplemental Material [24]). The phonon dispersion was investigated by using the PHONOPY code [27] with a $3 \times 3 \times 1$ supercell based on the frozen-phonon method. The crystal orbital Hamilton population (COHP) and crystal orbital bond index (COBI) were investigated by using the LOBSTER code [28–30]. Visualizations of structures were done with VESTA software [31].
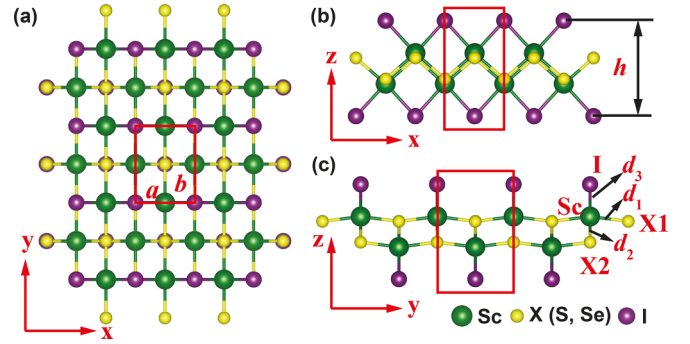
FIG. 1. The atomic structures of ScXI (X = S, Se) monolayers. (a) Top and (b,c) side views of the ScXI monolayers. The red rectangle with Bravais lattice vectors (a,b) is the corresponding primitive unit cell.

III. RESULTS AND DISCUSSION

A. Geometry and bonds characteristic

According to a previous experiment [12], bulk ScSI crystallizes in the FeOCl structure type with space group *Pmmn* [No. 59, $a = 3.8904(2)$, $b = 5.0732(9)$, $c = 8.9574(6)$ Å]. To quantitatively evaluate the feasibility of peeling off an atomic layer from the surface of a bulk material, we calculated the exfoliation energies (E_{exf}) according to the method of Ref. [32]. The E_{exf} of the ScSI monolayer is 13.78 meV/Å^2, which is smaller than that of typical experimentally synthesized monolayer 2D materials (e.g., phosphorene, graphene, MoS$_2$, and h-BN; see Fig. 2 in the Supplemental Material [24]). Our results validate the experimental speculation that bulk ScSI is readily exfoliable. The ScSeI monolayer also shows a similar small E_{exf} of 14.46 meV/Å^2. Figure 1 shows the atomic structures of ScXI (X = S, Se) monolayers, which belong to the rectangular Bravais lattice with *Pmmn* space group. The (ScX)$_n$ sheets, which are formed by lightly distorted, half-edge-sharing [ScX_4I$_2$]$^{7-}$ octahedra, sandwiched between the iodine layers. Each Sc atom forms six bonds with four S atoms and two I atoms, respectively. The difference of atomic size leads to the deviation of the bond length from that of a perfect octahedron. The bond lengths of the two Sc-I bonds are the same while the four Sc-X bonds are divided into two types according to different bond lengths [d_1 and d_2 in Fig. 1(c)].
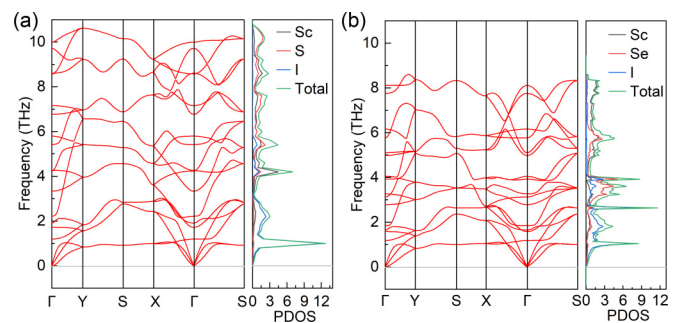
FIG. 2. Phonon dispersion curves and projected phonon density of states (DOS) of (a) ScSI and (b) ScSeI monolayers.

TABLE II. Calculated in-plane elastic stiffness constants, Young's modulus $E(\theta)$ (in units of N/m), and Poisson's ratio $\nu(\theta)$ of ScXI ($X =$ S, Se) monolayers.

System	C_{11}	C_{22}	C_{12}	C_{66}	$E(\theta)$ Max	$E(\theta)$ Min	$\nu(\theta)$ Max	$\nu(\theta)$ Min
ScSI	67.1	93.7	12.3	21.0	91.5	56.5	0.37	0.13
ScSeI	60.4	78.9	10.12	18.76	77.16	50.2	0.35	0.13
Graphene [34]	349	349	72	138	334.1	333.4	0.21	0.21
h-BN [35]	289.8	289.8	63.7	113.1	276	276	0.22	0.22
MoS$_2$ [36]	128.8	127.9	28.8	50.0	122.3	122.3	0.22	0.22
Phosphorene [37]	105	26	18	22	92.5	23.0	0.70	0.07

Other than E_{exf}, we further investigated the cohesive energy, mechanical stability, and lattice dynamic stability of ScXI monolayers. The negative cohesive energies (see Table I) indicate that ScXI monolayers are energetically stable. The calculated elastic constants (see Table II) of ScXI monolayers meet the Born criteria ($C_{11} > 0$ and $C_{66} > 0$) [35], which implies that they are mechanically stable in the rectangular lattice. Finally, the phonon dispersions of ScXI monolayers show no negative frequency (see Fig. 2), indicating their dynamical stability. The optimized structural parameters of ScXI monolayers are summarized in Table I. Compared to ScSeI, ScSI monolayer shows the small lattice constants and bond lengths, which is attributed to the difference of the ionic radius at the X-site elements.

To elucidate such a low value of E_{exf} in ScXI monolayers, we further investigated their chemical bonding characteristics. The electron localization function (ELF) along the (010) and (100) planes for ScXI monolayers is shown in Figs. 3(a) and 3(e), respectively. It can clearly be seen that X/I ($X =$ S and Se) and Sc atoms have, respectively, the highest and lowest ELF values, indicating that Sc donates its electrons to the system while X/I ($X =$ S and Se) gains electrons. The ELF profiles along the Sc-I and Sc-X bonds of ScXI monolayers were further investigated, as shown in Figs. 3(b) and 3(f). The ELF profiles along the Na-Cl bond of NaCl and the C-C bond of diamond were also provided as a reference for typical ionic and covalent bonds, respectively. It can be noticed that the ELF values in the region near the cationic nucleus are very low (below 0.01), while the ELF values in the region near the anionic nucleus are high, which demonstrates ionic bonding characteristics (e.g., Sc-I and Sc-X bonds) similar to the Na-Cl bond. The crystal orbital Hamilton population (COHP) and crystal orbital bond indices (COBIs) curves of ScXI monolayers are shown in Figs. 3(c), 3(g) and Figs. 3(d), 3(h), which is an intuitive way to quantify covalent bonds in solid-state materials. The integrated COHP (ICOHP) can be used as a measure of bond energy. In Figs. 3(c), 3(g), and Figs. 3(d), 3(h), red values are the absolute ICOHP values of Sc-I and Sc-X bonds in ScXI monolayers. It can be seen that the interactions between Sc-I and Sc-X bonds of ScXI monolayers are stronger than the typical Na-Cl ionic bond, but significantly weaker than the typical C-C covalent bond. On the other hand, the integrated COBI (ICOBI) of the Sc-I and Sc-X bonds are all $\sim$0.5, locating between 0.09 (Na-Cl)
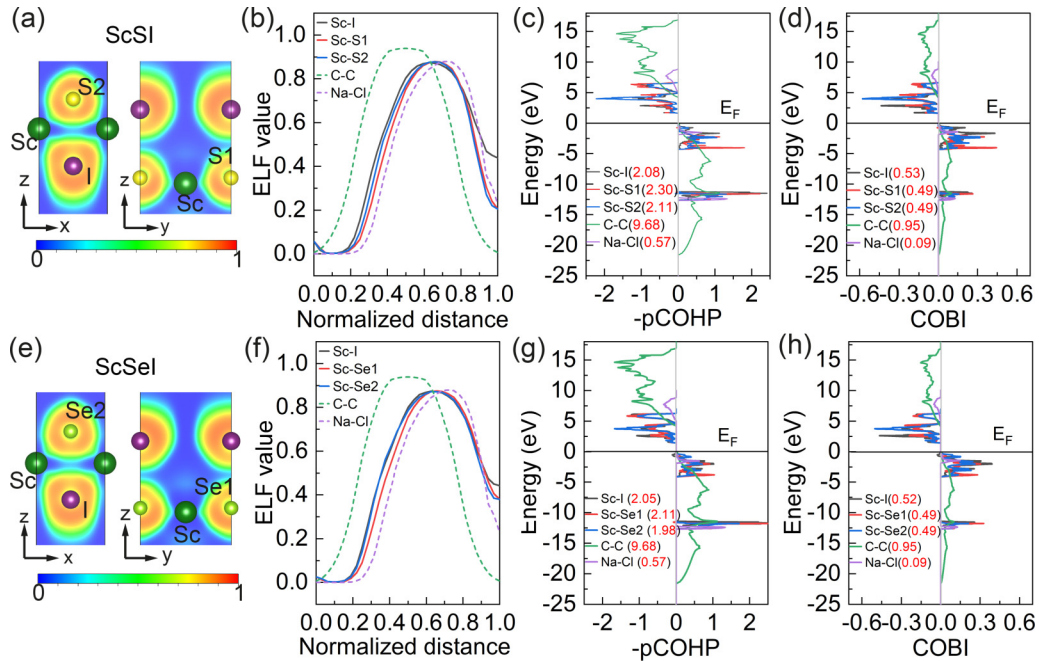
FIG. 3. Chemical bonding nature of ScXI ($X =$ S, Se) monolayers. The upper plane is ScSI monolayer and the bottom plane is ScSeI monolayer. (a), (e) 2D ELF along (010) and (100) planes. (b), (f) The ELF profiles along the Sc–I and Sc-X bonds. The ELF profiles along the Na-Cl bond of ionic crystal NaCl and the C-C bond of covalent crystal diamond as a reference for ionic and covalent bonds, respectively. (c), (g) Crystal orbital Hamilton Population (COHP) of Sc-I and Sc-X bonds. (d), (h) Crystal orbital bond indices (COBIs) of Sc-I and Sc-X bonds. COHPs and COBIs of NaCl and diamond are given for a purely covalent element and a strongly ionic material with negligible covalency, respectively. Absolute values in brackets are corresponding and integrated crystal orbital Hamilton population (ICOHP) and integrated crystal orbital bond indices (ICOBIs).
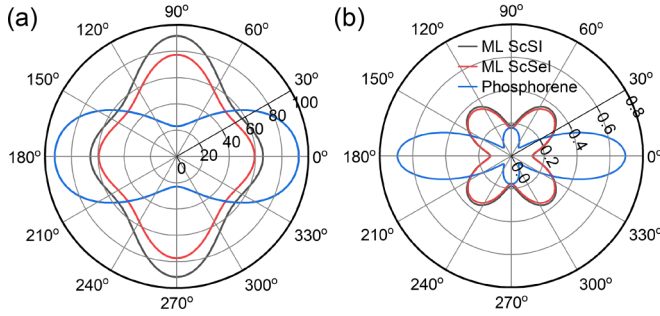
FIG. 4. Calculated orientation-dependent (a) Young's modulus $E(\theta)$ and (b) Poisson's ratio $\nu(\theta)$ of ScXI (X = S, Se) monolayers.

and 0.95 (C-C). Based on these results, we can conclude that the Sc-I and Sc-X bonds in ScXI monolayers show the mixed covalent-ionic bond characteristics, which is very similar to the soft Pb-X (X = halogen) chemical bond in typical halide perovskites [33].

B. Mechanical properties

Next, we discuss the mechanical properties of ScXI (X = S, Se) monolayers. The in-plane elastic stiffness constants, the minimum and maximum of Young's modulus, and Poisson's ratio for ScXI monolayers and typical 2D materials are summarized in Table II. It can be seen that the Young's moduli of ScXI monolayers are comparable to those of phosphorene (26–$105\,\mathrm{N\,m^{-1}}$), but smaller than those of graphene ($349\,\mathrm{N\,m^{-1}}$), MoS$_2$ ($122.3\,\mathrm{N\,m^{-1}}$), and h-BN ($276\,\mathrm{N\,m^{-1}}$), indicating the lower stiffness of the ScXI monolayers. In addition, it can be seen that the Young's modulus of the ScSI monolayer is slightly higher than that of the ScSeI monolayer, which is attributed to a stronger Sc-S bond (ICOHP = –2.21 eV) than the Sc-Se bond (ICOHP = –2.08 eV). The Poisson's ratio is a parameter that quantitatively represents the transverse deformation of a material in the direction perpendicular to the specific direction of loading. For the Poisson's ratio [see Fig. 4(b)], the maximum value and minimum value of ScXI (X = S, Se) monolayers are along the x axis and the along the diagonal direction, respectively, exhibiting remarkable anisotropy.

To investigate the elastic anisotropy of ScXI monolayers, we also calculated the orientation-dependent Young's moduli $E(\theta)$ and Poisson's ratio $\nu(\theta)$ based on Table II; $\theta \in [0, 2\pi]$ is the angle with respect to the $+x$ axis, as shown in Figs. 4(a) and 4(b). The related formulas [38] are as follows:

$$E(\theta) = \frac{Y_{zz}}{\cos^4\theta + d_2\cos^2\theta\sin^2\theta + d_3\sin^4\theta}, \quad (1)$$

$$\nu(\theta) = \frac{\nu_{zz}\cos^4\theta - d_1\cos^2\theta\sin^2\theta + \nu_{zz}\sin^4\theta}{\cos^4\theta + d_2\cos^2\theta\sin^2\theta + d_3\sin^4\theta}, \quad (2)$$

where

$$d_1 = \frac{C_{11}}{C_{22}} + 1 - \frac{C_{11}C_{22} - C_{12}^2}{C_{22}C_{66}},$$

$$d_2 = -\left(2\frac{C_{12}}{C_{22}} - \frac{C_{11}C_{22} - C_{12}^2}{C_{22}C_{66}}\right), \quad d_3 = \frac{C_{11}}{C_{22}}, \quad (3)$$

TABLE III. Summary of the ideal tensile strength, critical strains, and failure mechanisms of the ScXI (X = S, Se) monolayers under two strain paths (x and y directions). The data of graphene, h-BN, MoS$_2$, and phosphorene were provided for comparison.

	Direction	f (N/m)	Critical strain	Failure mechanism
ScSI	x	8.97	0.29	Phonon instability
	y	6.19	0.18	Phonon instability
ScSeI	x	8.11	0.33	Phonon instability
	y	4.84	0.18	Phonon instability
Graphene [39]	Zigzag	40.41	0.266	Elastic instability
	Armchair	36.74	0.194	Elastic instability
h-BN [40]	Zigzag	26.26	0.30	—
	Armchair	23.56	0.18	—
MoS$_2$ [41]	Zigzag	14.75	0.256	Phonon instability
	Armchair	9.59	0.18	Elastic instability
Phosphorene [42]	Zigzag	9.99	0.27	—
	Armchair	4.44	0.33	—

$$Y_{zz} = \frac{C_{11}C_{22} - C_{12}^2}{C_{22}}, \quad \nu_{zz} = \frac{C_{12}}{C_{22}}. \quad (4)$$

From Fig. 4(a), the Young's modulus of the ScXI (X = S, Se) monolayers varies from 56.5 to $91.5\,\mathrm{N\,m^{-1}}$ and from 50.2 to $77.16\,\mathrm{N\,m^{-1}}$, which shows the obvious anisotropy. It is also obvious that 2D projection plots of orientation-dependent Poisson's ratio of ScXI monolayers are basically coincident; the Poisson's ratio of ScSI monolayer is only slightly higher than that of the ScSeI monolayer, which is due to structural similarity and slight difference in bond strength. Meanwhile, these positive values mean that ScXI (X = S, Se) monolayers expand (contract) laterally under compressive (tensile) strains. Compared with typical 2D materials, the Poisson's ratio of graphene, MoS$_2$, and h-BN show isotropy but phosphorene exhibits stronger anisotropy.

To investigate plastic properties, stress-strain curves of ScXI (X = S, Se) were calculated, as shown in Figs. 5(a) and 5(e). When applying uniaxial tensile strain along the x direction of ScXI (X = S, Se) monolayers, the stress increases gradually until it reaches the maximum value of $8.97\,\mathrm{N\,m^{-1}}$ at the strain of 29% for the ScSI monolayer and $8.11\,\mathrm{N\,m^{-1}}$ at the strain of 33% for ScSeI monolayers, respectively. In the y direction, the strains corresponding to the maximum stress of $6.19\,\mathrm{N\,m^{-1}}$ (ScSI monolayer) and $4.84\,\mathrm{N\,m^{-1}}$ (ScSeI monolayer) are all 18%. It can be seen that the ideal tensile strengths of the ScSI monolayer under two paths (x and y directions) are slightly larger than those of the ScSeI monolayers, which is attributed to a stronger Sc-S bond than the Sc-Se bond. The ideal tensile strength, critical strains, and failure mechanisms of ScXI (X = S, Se) monolayers under two paths (x and y directions) and comparison with graphene, h-BN, MoS$_2$, and phosphorene are summarized in Table III. It is worth noting that the failure mechanisms of ScXI (X = S, Se) monolayers under two strain paths (x and y directions) are all phonon instability. In addition, the tensile strength is equivalent to that of MoS$_2$ and phosphorene but far lower than that of graphene and h-BN.
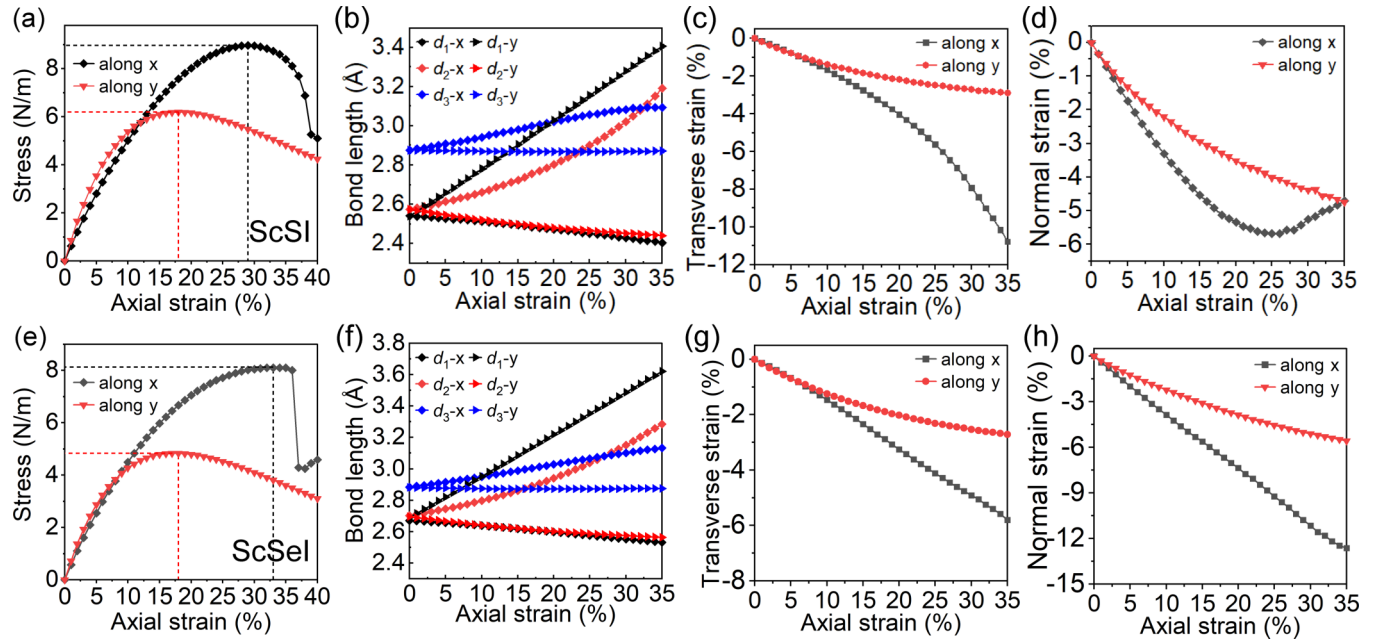
FIG. 5. (a–d) and (e–f) are stress-strain curves, bond length evolution, in-plane transverse strain evolution, and normal strain evolution along the x and y directions for ScSI and ScSeI monolayers, respectively.

The evolution of chemical bond lengths during tension reflects the nature of tensile strength. Therefore, we tracked the changes in chemical bonding during the stretching process. In Figs. 5(b) and 5(f), bond length evolutions for ScXI (X = S, Se) monolayers are shown. It is obvious that evolutions of d_1(Sc-X1 bond), d_2(Sc-X2 bond), and d_3(Sc-I bond) are basically consistent, which is due to the same structural configuration and similarity properties of X-site atoms. In addition, the projection of the Sc-X1 bond and the Sc-I bond on the xz plane forms a rhombuslike shape and the x direction is its diagonal [see Fig. 1(b)]. When applying uniaxial tensile strain along the x direction, the d_2 (Sc-X2 bond) near the vertical x direction is only slightly decreased due to the effect of Poisson's ratio while d_1(Sc-X1 bond) and d_3(Sc-I bond) on the side length of the rhombuslike shape [see Fig. 1(b)] are significantly increased. It is worth noting that the change of d_3(Sc-I bond) is weaker than that of d_2(Sc-X2 bond), which is because atoms of bounding iodine layers have a larger variation range to resist the influence of tensile strain along the x direction. When applying uniaxial tensile strain along the y direction, d_3(Sc-I bond) is basically unchanged and d_2(Sc-X2 bond) is slightly decreased. This is because the Sc-I bond is perfectly perpendicular to the y direction [see Fig. 1(c)]. In addition, the effect of bounding iodine layers also suppresses the influence of tensile strain along the x direction. Evolution of d_1(Sc-X1 bond) is linearly increased, similarly, which is because the Sc-X1 bond is parallel to the tensile direction x direction.

In-plane transverse strain evolution along the x and y directions for ScSI and ScSeI monolayers is shown in Figs. 5(c) and 5(g). It is clear that with the increase of tensile strain along $x(y)$, in-plane transverse strain also increases, which indicates that ScXI (X = S, Se) monolayers all have a positive Poisson's ratio, consistent with the analysis of elastic anisotropy for Poisson's ratio. In addition, the strain continuously increases

beyond the elastic stage; the effect of Poisson's ratio along x tensile direction is stronger than that along y tensile direction for ScXI (X = S, Se) monolayers. In order to describe the change of buckling height with the strain applied along the x or y direction, the out-of-plane Poisson's ratio [43] is defined as

$$\upsilon_{zx} = -\frac{\varepsilon_{zz}}{\varepsilon_{xx}}, \quad \upsilon_{zy} = -\frac{\varepsilon_{zz}}{\varepsilon_{yy}}, \tag{5}$$

where υ_{zx} (υ_{zy}) is the out-of-plane Poisson's ratio along the z axis when the stress is applied along the $x(y)$ direction, $\varepsilon_{zz} = (h-h_0)/h_0$ is the strain along the z axis, and h and h_0 are the buckling heights of strained and unstrained structures. In Figs. 5(d) and 5(h), normal strain evolution along the x and y directions for ScSI and ScSeI monolayers is shown, respectively. According to Eq. (5), υ_{zx} and υ_{zy} of ScSI monolayer are 0.35 and 0.26 in the elastic range, which is basically consistent with υ_{zx}(0.38) and υ_{zy}(0.24) of the ScSeI monolayer, respectively. It is also obvious that υ_{zx} is larger than υ_{zy} for ScXI (X = S, Se) monolayers, which is because the projection of the Sc-X1 bond and the Sc-I bond on the xz plane forms a rhombuslike shape and the x direction is its diagonal, while the Sc-I bond is perfectly perpendicular to the y direction.

C. Electronic properties

Electronic structure analysis has been widely adopted as an effective tool to shed light on the basic properties of semiconductors at the atomic level [44]. Band structures of ScSI and ScSeI monolayers are depicted in Figs. 6(a) and 6(d), respectively. It can be seen that ScSI and ScSeI monolayers show indirect band gaps (E_g) of 2.15 and 1.83 eV, respectively. The valence band maximum (VBM) of the ScSI and ScSeI monolayers is located at the Γ point, while the conduction band minimum (CBM) of the ScSI monolayer is located between the Γ-X points and the CBM of the ScSeI monolayer
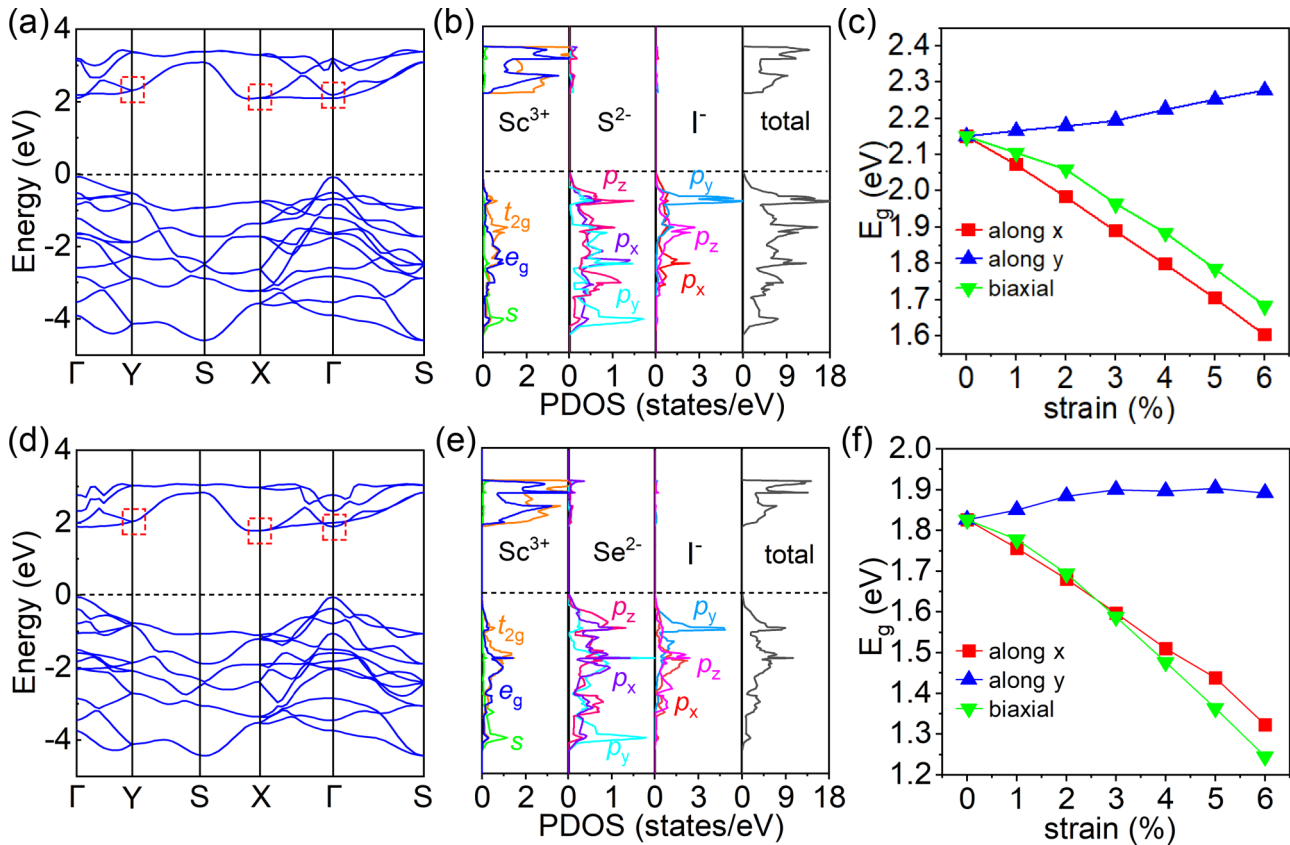
FIG. 6. (a–c) and (d–f) are band structure, projected density of states (PDOS), and band gap as a function of biaxial compressive strain using the HSE06 method for ScSI and ScSeI monolayers, respectively. The dotted line represents the Fermi energy level.

is located at the X point. The band gap reduction caused by replacing S in the ScSI monolayer with Se is mainly due to the higher energy level of the Se $4p$ orbital compared to the S $3p$ orbital. In addition, the energies of the conduction band at the high-symmetry points Γ, X, and Y (red dotted line box) are very close, which implies that the strain may be able to modulate the transition from the indirect band gap to the direct band gap by adjusting the energy difference between the Γ, X, and Y points. On the other hand, many energy valleys with high degeneracy are highly desired in thermoelectric (TE) materials [9]. Figures 6(b) and 6(e) show the projected density of states (PDOS) of ScSI and ScSeI monolayers, respectively. It is obvious that the CBMs are dominant due to the Sc $3d$ states, while the VBMs are mainly contributed by p_z states of X (S, Se) and p_y states of I. The ScSeI monolayer exhibits a slightly larger valence band dispersion compared to the ScSI monolayer due to the increased Sc d-Se p_z and Sc d-I p_y orbital hybridization.

Since the E_g of ScXI (X = S, Se) is still large relative to the required band gap for optoelectronic applications, strain is used as an effective means to reduce their E_g. As shown in Figs. 6(c) and 6(f), when applying compressive strain (from 0% to 6%) along the x and biaxial directions, the E_g of ScSI (ScSeI) monolayers shows a linear decreasing trend from 2.15 eV to 1.60 and 1.68 eV (from 1.83 eV to 1.32 and 1.24 eV), respectively. While when applying compressive strain along the y direction, the E_g of the ScSI (ScSeI) monolayer only has a slight increase from 2.15 to 2.28 eV (from 1.83 to 1.89 eV).

In addition to adjusting the band gap, the external strains can also induce the shifts of band edges. When a uniaxial compressive strain along the x direction and biaxial compressive strain are applied, the band gap types of the ScSI and ScSeI monolayers change from indirect ban band gap dgap to direct band gap while the compressive strains along the y direction do not change the indirect band gap nature of the ScSI and ScSeI monolayers.

To further understand the evolution of the band gap under different strain state, band alignment relative to the vacuum energy level is performed for VBM and CBM. Figures 7(a)–7(c) and Figs. 7(d)–7(f) are the energy of the VBM and CBM relative to the vacuum potential at the HSE06 level, under uniaxial strain along x, uniaxial strain along y, and biaxial strain for ScSI and ScSeI monolayers, respectively. It is obvious that when compressive strain is applied along the x direction and biaxial directions, the positions of the CBMs for ScSI and ScSeI monolayers are not basically changed with increase of the compressive strains while the positions of the VBMs keep moving up with increase of the compressive strains, which leads to a reduction in the band gap with increase of the compressive strains. When compressive strain is applied along the y direction, the positions of the VBMs and CBMs for ScSI and ScSeI monolayers are slightly changed with increase of the compressive strains. Uniaxial and biaxial compressive strains can effectively regulate the orbital hybridization states between the d orbital of Sc and the p orbital of the elements at the X and I sites, inducing change of the band gap of ScXI
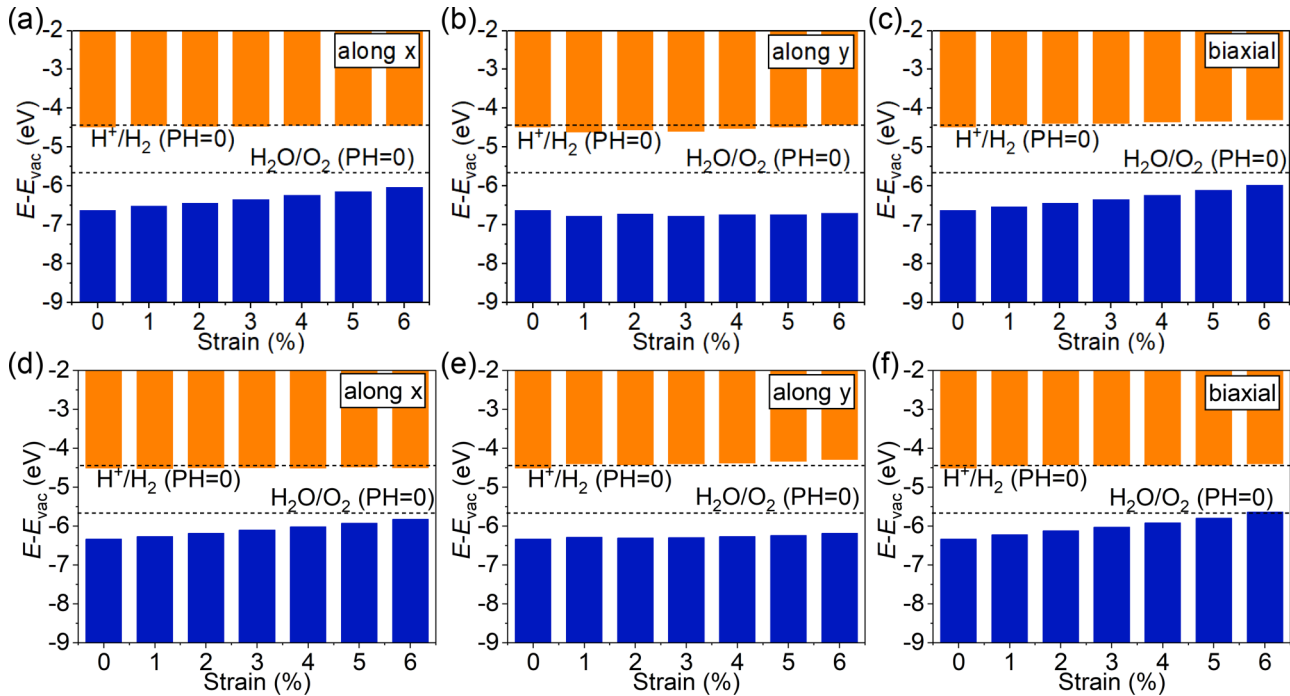
FIG. 7. (a–c) and (d–f) are the energy of the VBM and CBM relative to vacuum potential at HSE06 level of ScXI (X = S, Se) under uniaxial strain along x, uniaxial strain along y, and biaxial strain for ScSI and ScSeI monolayers, respectively. CBM and VBM are marked as blue and brown, respectively.

(X = S, Se) monolayers. In addition, the band edge alignments of the ScXI (X = S, Se) monolayers have been depicted and compared with the oxidation potential of H_2O/O_2 (-5.66 eV, $pH = 0$) and the reduction potential H^+/H_2 (-4.44 eV, $pH = 0$) [45]. As shown in Fig. 7, the band edge positions of ScXI (X = S, Se) monolayers at different strain states have been depicted and aligned with the oxidation potential of H_2O/O_2 (-5.66 eV, $pH = 0$) and the reduction potential H^+/H_2 (-4.44 eV, $pH = 0$). Under strain-free condition, the VBMs of ScXI (X = S, Se) are lower than the oxidation potential of H_2O/O_2, while the CBMs of ScXI (X = S, Se) are slightly lower than the reduction potential of H^+/H_2, which does not meet the basic conditions for photocatalytic water splitting at $pH = 0$ [46]. When a biaxial compressive strain of 4%–6% is applied to the ScSI monolayer or a uniaxial strain of 4%–6% is applied to the ScSeI monolayer along the y direction, their CBMs shift upward, which can make their CBM energy levels slightly higher than the reduction potential of H^+/H_2. Therefore, strain engineering can make ScXI (X = S, Se) monolayers promising for meeting the basic conditions for photocatalytic water splitting at $pH = 0$.

D. Vertical and lateral heterostructures

Heterostructure design can engineer the electronic properties of semiconductors, which has been proven to be an effective method [47–49]. Conduction and valence band edges relative to vacuum potential at HSE06 and PBE levels for ScXI (X = S, Se) monolayers and some typical 2D semiconductors are shown in Fig. 8. Relative to the vacuum level (E_{vac}), the VBM and CBM of ScSeI monolayer are -6.33 and -4.50 eV at the HSE06 level (-6.13 and -4.44 eV at the PBE level).

In addition to the ScSI monolayer, the VBM and CBM are -6.62 and -4.47 eV at the HSE06 level (-6.13 and -4.44 eV at the PBE level). Compared to other typical 2D semiconductors, their VBMs and CBMs are all lower than those of typical 2D semiconductors, respectively, implying that type II vertical heterostructure can be formed between ScXI (X = S, Se) monolayers and these typical 2D semiconductors. In addition, it is noteworthy that type II band alignments are very useful for unipolar electronic device applications since
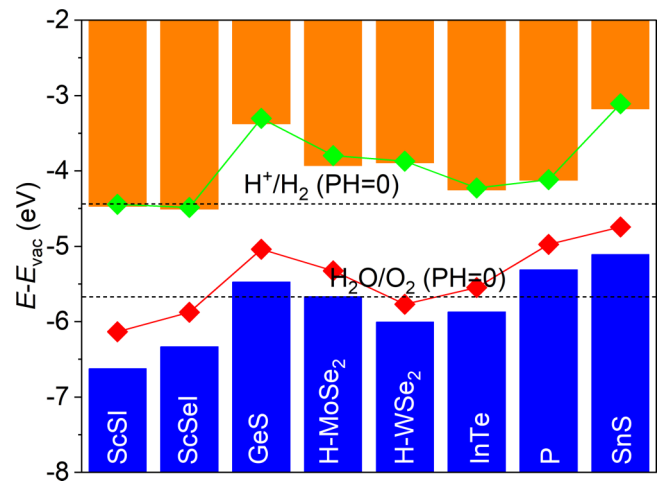
FIG. 8. Conduction and valence band edges relative to vacuum potential at HSE06 and PBE level for the 2D crystals. CBM and VBM for HSE06 level are marked as blue and brown, respectively. CBM and VBM for PBE level are marked as green and red, respectively.
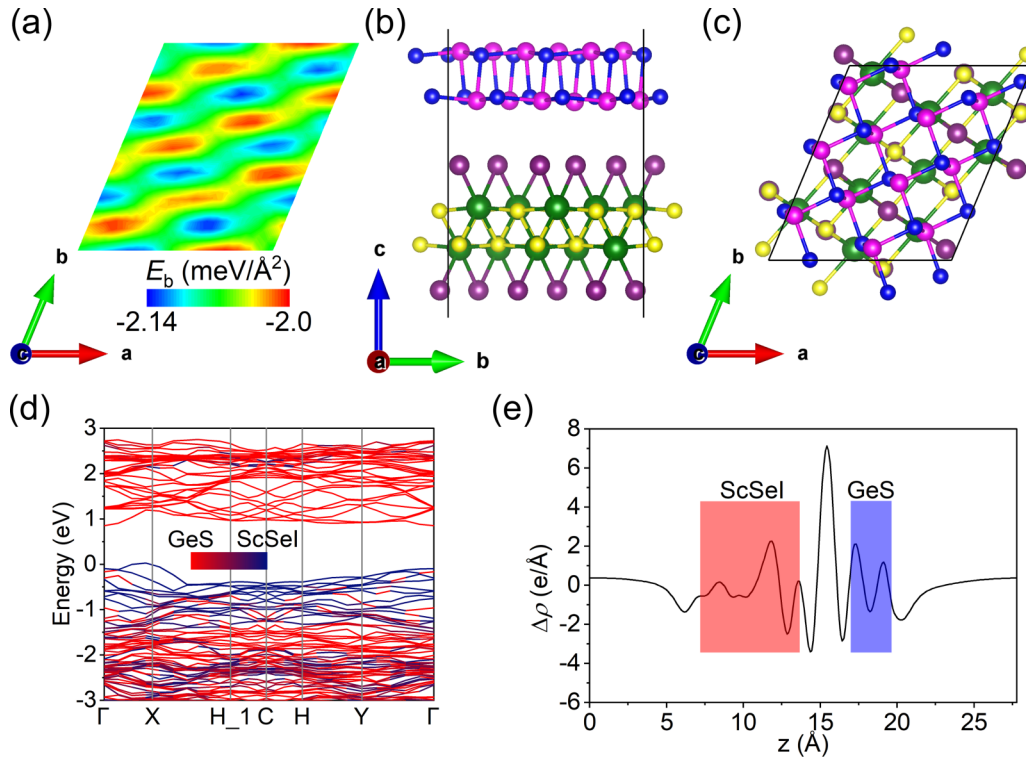
FIG. 9. (a) Energy surface of E_b of ScSeI/GeS heterostructure with a series of configurations. (b) Side view and (c) top view of GeS/ScSeI heterostructure with minimum of E_b. (d) Band structure of corresponding ScSeI/GeS heterostructure at HSE06 level. (e) Plane-averaged charge density difference $\Delta\rho(z)$ of corresponding ScSeI/GeS heterostructure. Sc, Se, I, S, and Ge atoms are displayed in green, yellow, purple, blue, and pink, respectively.

they allow larger offsets on one side (either conduction or valence band), thus allowing extremely strong carrier confinement [50]. Among the 2D materials we investigated, only the CBMs and VBMs (HSE06 level) of H-WSe$_2$ and InTe monolayers satisfy the basic conditions (i.e., CBMs are higher than the reduction potential of H$^+$/H$_2$ and VBMs are lower than the oxidation potential of H$_2$O/O$_2$), which is promising for the application of photocatalytic water splitting (pH = 0).

To verify our speculation, ScSeI and GeS monolayers were chosen as a typical example to investigate electronic properties of their vertical heterostructure (VH). Herein, some tools of JARVIS Heterostructure [51] were employed to generate suitable 2D ScSeI/GeS VH, whose lattice mismatch of 2D ScSeI/GeS VH is less than 2%, indicating that the strain effects on the electronic properties are very little and can be neglected. For the interface model, different stacking types between ScSeI and GeS monolayers can produce a series of interface configurations. To confirm the thermodynamic stability of the most stable heterostructure among all configurations, binding energies E_b were calculated by the following equation [52],

$$E_b = E_{A/B} - E_A - E_B, \quad (6)$$

where $E_{A/B}$, E_A, and E_B represent the total energy of A/B heterostructure, components A and B, respectively. We calculate the binding energy E_b for different relative positions of two monolayers, ScSeI and GeS, obtaining in this way a sampling of the energy surface of E_b, as shown in Fig. 9(a). Negative E_b for all patterns also suggests that the fabrication of ScSeI/GeS

VH is energetically feasible. Simultaneously, the smaller the E_b, the more stable the configuration of ScSeI/GeS VH. Based on the energy surface of E_b of ScSeI/GeS VH, the most stable configuration with minimum E_b (−2.14 meV/Å^2) is obtained, as shown in Figs. 9(b) and 9(c). For the most stable configuration obtained, its band structure is investigated to determine the band type of ScSeI/GeS VH as shown in Fig. 9(d). It is obvious that CBM is contributed by ScSeI while VBM is contributed by GeS, meeting the apparent feature of type II heterostructure, which confirms our speculation. It is worth noting that type II band alignments are very useful for unipolar electronic device applications since they allow larger offsets on one side (either conduction or valence band), thus allowing extremely strong carrier confinement [50]. In order to analyze the charge transfer in the type II ScSeI/GeS VH, we plot plane-averaged charge density difference $\Delta\rho(z)$ along the direction perpendicular to the interface (z axis) in Fig. 9(e). It can be seen that the charge redistribution is very obvious near the interface and a large number of electrons ($10^{-1}\,e$) gather at the interface, which enhances interface interaction.

Moreover, the electronic properties of lateral heterostructure (LH) composed of ScSeI and ScSeBr monolayers have also been studied. Here, (ScSeI)$_3$/(ScSeBr)$_3$ LH along the x and y directions, abbreviated as (ScSeI)$_3$/(ScSeBr)$_3$(x) and (ScSeI)$_3$/(ScSeBr)$_3$(y) LHs, are selected to investigate the electronic properties of (ScSeI)$_m$/(ScSeBr)$_n$ LHs, as shown in Fig. 10(a). First, the E_b of (ScSeI)$_3$/(ScSeBr)$_3$(x) and (ScSeI)$_3$/(ScSeBr)$_3$(y) LHs are −8.06 and −2.70 eV, respectively, indicating that they are thermodynamically sta-
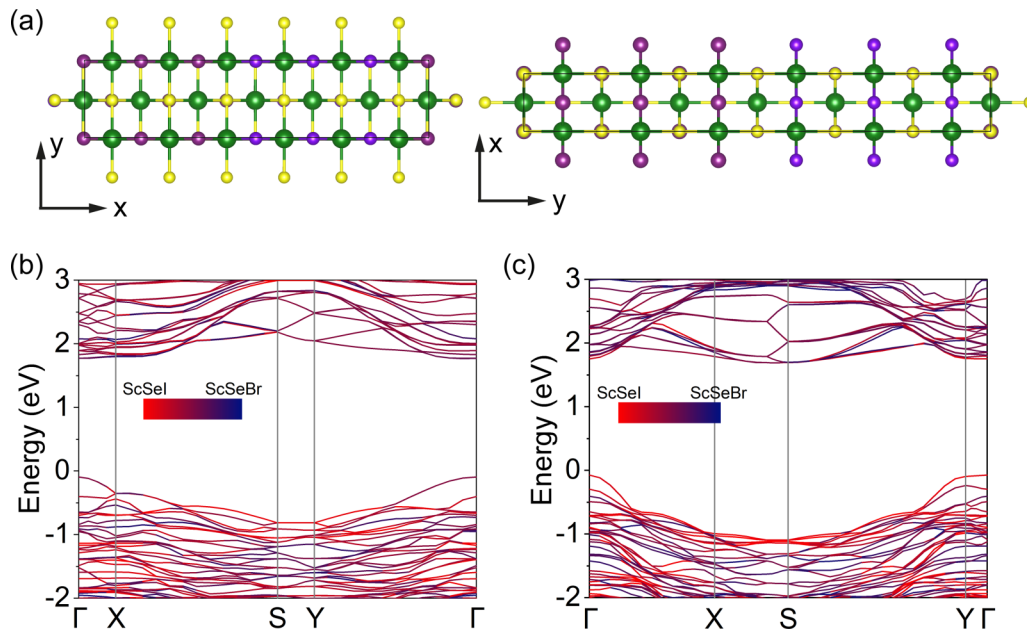
FIG. 10. (a) Top view of atomic configurations of $(ScSeI)_3/(ScSeBr)_3$ LHs along the x and y directions, respectively. (b,c) are HSE06 band structures of $(ScSeI)_3/(ScSeBr)_3$ LHs along the x and y directions, respectively. Sc, Se, I, and Br atoms are displayed in green, yellow, purple, blue, and bluish purple, respectively.

ble. Meanwhile, it can be found that $(ScSeI)_3/(ScSeBr)_3(x)$ LH shows higher stability than $(ScSeI)_3/(ScSeBr)_3(y)$ LH. Figures 10(b) and 10(c) show band structures of $(ScSeI)_3/(ScSeBr)_3(x)$ and $(ScSeI)_3/(ScSeBr)_3(y)$ LHs, respectively. On the one hand, it can be seen that $(ScSeI)_3/(ScSeBr)_3(x)$ and $(ScSeI)_3/(ScSeBr)_3(y)$ LHs are both indirect-gap semiconductors with band gaps of 1.87 and 1.77 eV, respectively. On the other hand, we can see that the VBM and CBM of $(ScSeI)_3/(ScSeBr)_3(x)$ and $(ScSeI)_3/(ScSeBr)_3(y)$ LH are contributed by ScSeI, demonstrating type I heterostructure, which can be utilized in optical devices, such as light-emitting diodes (LEDs) [50].

IV. CONCLUSION

In summary, we have systematically investigated the structural, mechanical, and electronic properties of ScXI ($X =$ S, Se) monolayers using first-principles calculations. It is found that exfoliation energies of ScXI ($X =$ S, Se) monolayers (13.78 and 14.46 meV/Å^2) are far smaller than some typical 2D semiconductors such as phosphorene, graphene, MoS_2, and h-BN. Unlike the covalent bonds in typical 2D materials, the soft Sc-X and Sc-I bonds with the mixed covalent-ionic bond characteristics are responsible for their low exfoliation energies. Based on the calculated cohesive energy, elastic constants, and phonon dispersion, ScXI ($X =$ S, Se) monolayers are stable. The Young's moduli (50.2–91.5 N m^{-1}) of ScXI monolayers are comparable to those of phosphorene (26–105 N m^{-1}), but smaller than those of graphene (349 N m^{-1}), MoS_2 (122.3 N m^{-1}), and h-BN (276 N m^{-1}), indicating the lower stiffness of the ScXI

monolayers. In addition, the ScSI/ScSeI monolayer shows remarkable elastic anisotropy and good flexibility (critical strain of 29%/33%). Electronic structure calculations show that ScSI/ScSeI monolayers have large indirect bandgaps (2.15/1.83 eV). Compressive strain can regulate the band gap and band edge of ScSI/ScSeI monolayers. For instance, the band gap of the ScSeI monolayer decreases from 1.83 to 1.51 eV and the band gap type changes from indirect band gap to direct band gap when the compressive strain along the x direction is 6%, which is attributed to the orbital hybridization between the d orbital of Sc and p orbital of the elements at the X and I sites. Taking ScSeI as an example, ScSeI/GeS vertical and $(ScSeI)_3/(ScSeBr)_3$ lateral heterostructures were built. Type I and type II band alignments can be observed in these heterostructures, which can provide valuable guidance for unique device applications.

[1] K. S. Novoselov, A. K. Geim, S. V. Morozov, D. Jiang, Y. Zhang, S. V. Dubonos, I. V. Grigorieva, and A. A. Firsov, Electric field effect in atomically thin carbon films, Science **306**, 666 (2004).

[2] P. Kumar, V. Sharma, S. N. Shirodkar, and P. Dev, Predicting phase preferences of two-dimensional transition metal dichalcogenides using machine learning, Phys. Rev. Mater. **6**, 094007 (2022).

[3] J. Linghu, T. Yang, Y. Luo, M. Yang, J. Zhou, L. Shen, and Y. P. Feng, High-throughput computational screening of vertical 2D van der Waals heterostructures for high-efficiency excitonic solar cells, ACS Appl. Mater. Interfaces **10**, 32142 (2018).

[4] K. F. Garrity, High-throughput first-principles search for new ferroelectrics, Phys. Rev. B **97**, 024115 (2018).

[5] L. Caputo, V. H. Nguyen, and J. C. Charlier, First-principles study of the structural and electronic properties of BN-ring doped graphene, Phys. Rev. Mater. **6**, 114001 (2022).

[6] X.-F. Zhou, A. R. Oganov, Z. Wang, I. A. Popov, A. I. Boldyrev, and H.-T. Wang, Two-dimensional magnetic boron, Phys. Rev. B **93**, 085406 (2016).

[7] X. F. Zhou, X. Dong, A. R. Oganov, Q. Zhu, Y. Tian, and H. T. Wang, Semimetallic Two-Dimensional Boron Allotrope with Massless Dirac Fermions, Phys. Rev. Lett. **112**, 085502 (2014).

[8] H. Qi, Z. Sun, N. Wang, G. Qin, H. Zhang, and C. Shen, Two-dimensional $Al_2I_2Se_2$: A promising anisotropic thermoelectric material, J. Alloys Compd. **876**, 160191 (2021).

[9] S. Z. Huang, Q. Y. Feng, B. Y. Wang, H. D. Yang, B. Li, X. Xiang, X. T. Zu, and H. X. Deng, Valley degeneracy-enhanced thermoelectric performance in In-based FeOCl-type monolayers, ACS Appl. Energy Mater. **5**, 13042 (2022).

[10] T. Zhang *et al.*, Magnetism and optical anisotropy in van der Waals antiferromagnetic insulator CrOCl, ACS Nano **13**, 11353 (2019).

[11] S. Yamanaka, K. Itoh, H. Fukuoka, and M. Yasukawa, High-pressure synthesis of the polymorph of layer structured compounds MNX (M = Zr, Hf; X = Cl, Br, I), Inorg. Chem. **39**, 806 (2000).

[12] A. M. Ferrenti, M. A. Siegler, S. Gao, N. Ng, and T. M. McQueen, ScSI: A new exfoliatable semiconductor, Chem. Mater. **34**, 5443 (2022).

[13] F.-Y. Xu, Y. Zhou, T. Zhang, Z.-Y. Zeng, X.-R. Chen, and H.-Y. Geng, An *ab initio* study of two-dimensional anisotropic monolayers ScXY (X = S and Se; Y = Cl and Br) for photocatalytic water splitting applications with high carrier mobilities, Phys. Chem. Chem. Phys. **24**, 3770 (2022).

[14] N. L. P. Andrews, J. Z. Fan, R. L. Forward, M. C. Chen, and H.-P. Loock, Electronic structure and interfacial contact with metallic borophene of monolayer ScSX (X = I, Br, and Cl), Phys. Chem. Chem. Phys. **19**, 73 (2017).

[15] Z. C. Xu, C. Y. Fong, F. Wooten, and Y. Yeh, Reflectance ellipsometry studies of the ternary chalcohalides SbSI, SbSeI and BiSI near room temperature, Ferroelectrics **56**, 187 (1984).

[16] G. Kresse and J. Furthmüller, Efficient iterative schemes for *ab initio* total-energy calculations using a plane-wave basis set, Phys. Rev. B **54**, 11169 (1996).

[17] G. Kresse and D. Joubert, From ultrasoft pseudopotentials to the projector augmented-wave method, Phys. Rev. B **59**, 1758 (1999).

[18] J. P. Perdew, K. Burke, and M. Ernzerhof, Generalized Gradient Approximation Made Simple, Phys. Rev. Lett. **77**, 3865 (1996).

[19] P. E. Blöchl, Projector augmented-wave method, Phys. Rev. B **50**, 17953 (1994).

[20] H. J. Monkhorst and J. D. Pack, Special points for Brillouin-zone integrations, Phys. Rev. B **13**, 5188 (1976).

[21] J. D. Pack and H. J. Monkhorst, "Special points for Brillouin-zone integrations"—a reply, Phys. Rev. B **16**, 1748 (1977).

[22] M. Dion, H. Rydberg, E. Schröder, D. C. Langreth, and B. I. Lundqvist, Van der Waals Density Functional for General Geometries, Phys. Rev. Lett. **92**, 246401 (2004).

[23] J. Klimeš, D. R. Bowler, and A. Michaelides, Van der Waals density functionals applied to solids, Phys. Rev. B **83**, 195131 (2011).

[24] See Supplemental Material at http://link.aps.org/supplemental/10.1103/PhysRevMaterials.7.014010 for one table: the calculated lattice parameters of bulk ScSI using different functional; and two figures: HSE band gap of bulk ScSI varying with mixing parameter (α); HSE band structure of bulk ScSI with and without SOC; and the n-layer exfoliation energies per area of $E_{exf}(n)$, of ScXI (X = S, Se).

[25] T. M. Henderson, J. Paier, and G. E. Scuseria, Accurate treatment of solids with the HSE screened hybrid, Phys. Status Solidi B **248**, 767 (2011).

[26] J. Heyd, J. E. Peralta, G. E. Scuseria, and R. L. Martin, Energy band gaps and lattice parameters evaluated with the Heyd-Scuseria-Ernzerhof screened hybrid functional, J. Chem. Phys. **123**, 174101 (2005).

[27] A. Togo and I. Tanaka, First principles phonon calculations in materials science, Scr. Mater. **108**, 1 (2015).

[28] S. Maintz, V. L. Deringer, A. L. Tchougréeff, and R. Dronskowski, LOBSTER: A tool to extract chemical bonding from plane-wave based DFT, J. Comput. Chem. **37**, 1030 (2016).

[29] S. Steinberg and R. Dronskowski, The crystal orbital Hamilton population (COHP) method as a tool to visualize and analyze chemical bonding in intermetallic compounds, Crystals **8**, 225 (2018).

[30] V. L. Deringer, A. L. Tchougréeff, and R. Dronskowski, Crystal orbital Hamilton population (COHP) analysis as projected from plane-wave basis sets, J. Phys. Chem. A **115**, 5461 (2011).

[31] K. Momma and F. Izumi, VESTA: A three-dimensional visualization system for electronic and structural analysis, J. Appl. Crystallogr. **41**, 653 (2008).

[32] J. H. Jung, C. H. Park, and J. Ihm, A rigorous method of calculating exfoliation energies from first principles, Nano Lett. **18**, 2759 (2018).

[33] H. Zhong, C. Feng, H. Wang, D. Han, G. Yu, W. Xiong, Y. Li, M. Yang, G. Tang, and S. Yuan, Structure–composition–property relationships in antiperovskite nitrides: Guiding a rational alloy design, ACS Appl. Mater. Interfaces **13**, 48516 (2021).

[34] G. Zhang, K. Lu, Y. Wang, H. Wang, and Q. Chen, Mechanical and electronic properties of $\alpha - M_2X_3$ (M = Ga, In; X = S, Se) monolayers, Phys. Rev. B **105**, 235303 (2022).

[35] R. C. Andrew, R. E. Mapasha, A. M. Ukpong, and N. Chetty, Mechanical properties of graphene and boronitrene, Phys. Rev. B **85**, 125428 (2012).

[36] K. Liu *et al.*, Elastic properties of chemical-vapor-deposited monolayer MoS_2, WS_2, and their bilayer heterostructures, Nano Lett. **14**, 5097 (2014).

[37] L. Wang, A. Kutana, X. Zou, and B. I. Yakobson, Electromechanical anisotropy of phosphorene, Nanoscale **7**, 9746 (2015).

[38] Z. Chen, H. Wang, and Z. Li, First-principles study of two dimensional C_3N and its derivatives, RSC Adv. **10**, 33469 (2020).

[39] F. Liu, P. Ming, and J. Li, *Ab initio* calculation of ideal strength and phonon instability of graphene under tension, Phys. Rev. B **76**, 064120 (2007).

[40] Q. Peng, W. Ji, and S. De, Mechanical properties of the hexagonal boron nitride monolayer: *Ab initio* study, Comput. Mater. Sci. **56**, 11 (2012).

[41] T. Li, Ideal strength and phonon instability in single-layer MoS_2, Phys. Rev. B **85**, 235407 (2012).

[42] H. Wang, Q. Li, Y. Gao, F. Miao, X. F. Zhou, and X. G. Wan, Strain effects on borophene: Ideal strength, negative Possion's ratio and phonon instability, New J. Phys. **18**, 073016 (2016).

[43] H. Zhong, K. Huang, G. Yu, and S. Yuan, Electronic and mechanical properties of few-layer borophene, Phys. Rev. B **98**, 054104 (2018).

[44] G. Tang, P. Ghosez, and J. Hong, Band-edge orbital engineering of perovskite semiconductors for optoelectronic applications, J. Phys. Chem. Lett. **12**, 4227 (2021).

[45] V. Chakrapani, J. C. Angus, A. B. Anderson, S. D. Wolter, B. R. Stoner, and G. U. Sumanasekera, Charge transfer equilibria between diamond and an aqueous oxygen electrochemical redox couple, Science **318**, 1424 (2007).

[46] V. Sharma, B. Bein, A. Lai, B. Pamuk, C. E. Dreyer, M. Fernández-Serra, and M. Dawber, Cooperative interactions between surface terminations explain photocat-

alytic water splitting activity on $SrTiO_3$, PRX Energy **1**, 023002 (2022).

[47] M. Seyedmohammadzadeh, C. Sevik, and O. Gülseren, Two-dimensional heterostructures formed by graphenelike ZnO and MgO monolayers for optoelectronic applications, Phys. Rev. Mater. **6**, 104004 (2022).

[48] Y. T. Ren, L. Hu, Y. T. Chen, Y. J. Hu, J. L. Wang, P. L. Gong, H. Zhang, L. Huang, and X.-Q. Shi, Two-dimensional MSi_2N_4 monolayers and van der Waals heterostructures: Promising spintronic properties and band alignments, Phys. Rev. Mater. **6**, 064006 (2022).

[49] H. Zhong, M. Yang, G. Tang, and S. Yuan, Type-II lateral heterostructures of monolayer halide double perovskites for optoelectronic applications, ACS Energy Lett. **5**, 2275 (2020).

[50] V. O. Özçelik, J. G. Azadani, C. Yang, S. J. Koester, and T. Low, Band alignment of two-dimensional semiconductors for designing heterostructures with momentum space matching, Phys. Rev. B **94**, 035125 (2016).

[51] K. Choudhary, K. F. Garrity, S. T. Hartman, G. Pilania, and F. Tavazza, Efficient computational design of 2D van der Waals heterostructures: Band-alignment, lattice-mismatch, web-app generation and machine-learning, arXiv:2004.03025.

[52] R. M. Pallares, X. Su, S. H. Lim, and N. T. K. Thanh, Fine-tuning of gold nanorod dimensions and plasmonic properties using the Hofmeister effects, J. Mater. Chem. C **4**, 53 (2016).